

Enabling High-Performance All-Solid-State Batteries via Guest Wrench in Zeolite Strategy

Xiwen Chi, Malin Li, Xiao Chen, Jun Xu, Xin Yin, Shanghua Li, Ziyue Jin, Zhaodi Luo, Xingxing Wang, Dechen Kong, Meng Han, Ji-Jing Xu, Zonghang Liu, Donghai Mei, Jiaao Wang,* Graeme Henkelman, and Jihong Yu*



Cite This: *J. Am. Chem. Soc.* 2023, 145, 24116–24125



Read Online

ACCESS |



Metrics & More

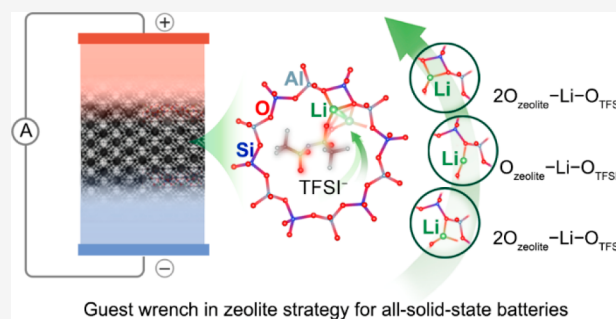


Article Recommendations



Supporting Information

ABSTRACT: All-solid-state batteries with a high energy density and safety are desirable candidates for next-generation energy storage applications. However, conventional solid electrolytes for all-solid-state batteries encounter limitations such as poor ionic conduction, interfacial compatibility, instability, and high cost. Herein, taking advantage of the ingenious capability of zeolite to incorporate functional guests in its void space, we present an innovative ionic activation strategy based on the “guest wrench” mechanism, by introducing a pair of cation and anion of LiTFSI-based guest species (GS) into the supercage of the LiX zeolite, to fabricate a zeolite membrane (ZM)-based solid electrolyte (GS-ZM) with high Li ionic conduction and interfacial compatibility. The restriction of zeolite frameworks toward the framework-associated Li ions is significantly reduced through the dynamic coordination of Li ions with the “oxygen wrench” of TFSI[−] at room temperature as shown by experiments and Car–Parrinello molecular dynamics simulations. Consequently, the GS-ZM shows an ~100% increase in ionic conductivity compared with ZM and an outstanding Li⁺ transference number of 0.97. Remarkably, leveraging the superior ionic conduction of GS-ZM with the favorable interface structure between GS-ZM and electrodes, the assembled all-solid-state Li-ion and Li–air batteries based on GS-ZM exhibit the best-level electrochemical performance much superior to batteries based on liquid electrolytes: a capacity retention of 99.3% after 800 cycles at 1 C for all-solid-state Li-ion batteries and a cycle life of 909 cycles at 500 mA g^{−1} for all-solid-state Li–air batteries. The mechanistic discovery of a “guest wrench” in zeolite will significantly enhance the adaptability of zeolite-based electrolytes in a variety of all-solid-state energy storage systems with high performance, high safety, and low cost.



INTRODUCTION

Reversible batteries with high energy density and safety are in increasing demand for clean energy storage systems.^{1,2} Although batteries based on liquid electrolytes (LEs) have achieved successful commercialization, the risks of leakage, combustion, volatilization, and decomposition of LEs remain a challenge for the safe and stable operation of batteries. To alleviate the issues of LEs mentioned above, growing efforts have been made to develop all-solid-state batteries based on solid electrolytes^{3,4} (SEs, Figure 1a). However, the currently available inorganic SEs with high ionic conductivity, mechanical strength, and safety such as garnets, NASICONs, and sulfides encounter limitations due to the instability against air components and metal anodes, poor interfacial compatibility, and high cost.^{5–7} In addition, polymer SEs^{8,9} and composite SEs based on LE confinement^{10,11} generally suffer from low transference number of metal-ion carriers (<0.5) as well as limited ionic conduction.

Moreover, the practical application of these SEs is hindered by their excessive thickness and mass, complicated preparation

process, and high cost.^{12,13} Therefore, developing all-solid-state energy storage systems with superior safety, desirable electrochemical performance, high energy density, and low cost based on highly adaptable SEs remains a great challenge.

Ion-conductive LiX zeolite membranes (ZMs) have emerged as a new class of inorganic SE with high stability and low cost,^{14,15} while ongoing research on the conductive mechanism and the construction of high interfacial compatibility for all-solid-state batteries are still in their infancy, and the electrochemical performance needs to be further improved. Taking advantage of the ingenious capability of zeolites to incorporate functional guests in its void space,¹⁶ herein, we present an innovative ionic activation strategy based on a

Received: July 22, 2023

Published: October 2, 2023



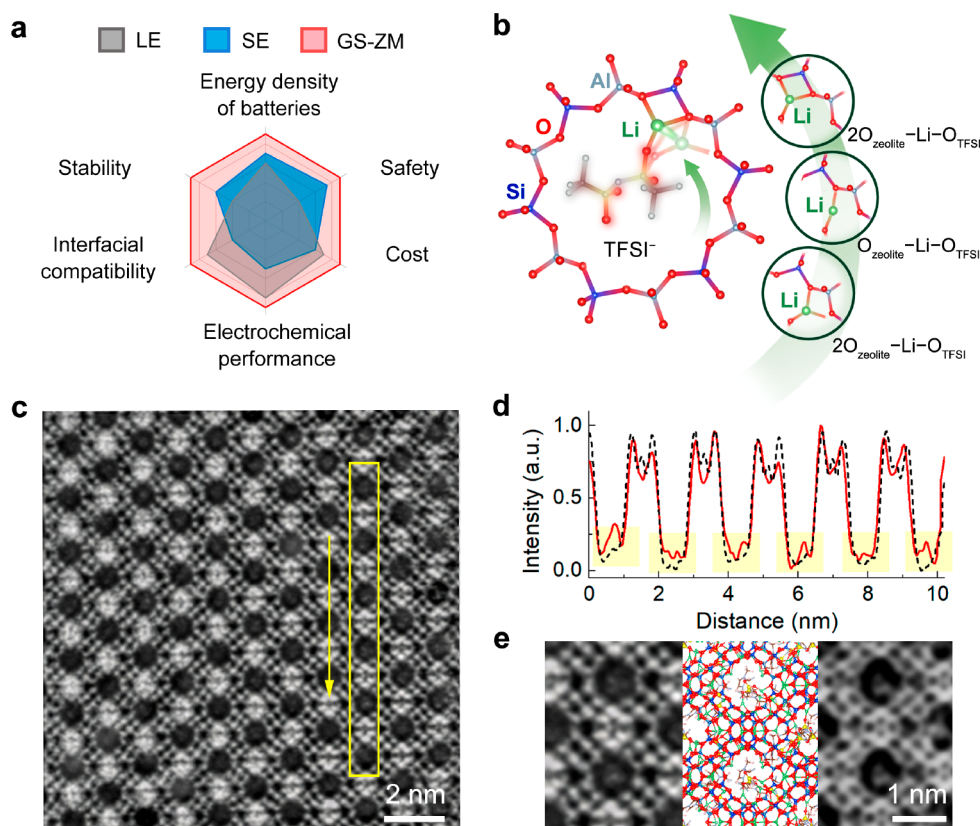


Figure 1. Design and fabrication of GS-ZM based on the “guest wrench” in zeolite strategy. (a) Radar plots of capabilities of LE, SE, and GS-ZM proposed in this work. (b) Schematic illustration for the activation process of framework-associated Li^+ in GS-ZM. The framework-associated Li^+ ions in the GS-ZM can be activated through the dynamic coordination with the “oxygen wrench” of TFSI^- at room temperature, which can reduce the restriction of zeolite frameworks toward the framework-associated Li^+ ions. For instance, Li^+ coordinated with two O of the zeolite and an O of the TFSI^- in GS (noted as $2\text{O}_{\text{zeolite}}-\text{Li}-\text{O}_{\text{TFSI}}$) is chosen as an initial configuration. Then, the coordination between the Li^+ and the O of the zeolite can be interrupted by the vibration of the TFSI^- forming the $\text{O}_{\text{zeolite}}-\text{Li}-\text{O}_{\text{TFSI}}$ transition state, and the Li^+ is dragged to a neighbor site, where the Li^+ coordinates with two O of the zeolite and an O of the TFSI^- , forming $2\text{O}_{\text{zeolite}}-\text{Li}-\text{O}_{\text{TFSI}}$. (c) IDPC-STEM image of GS-ZM. Scale bar: 2 nm. (d) Profile analysis (red solid line for GS-ZM, black dashed line for ZM) of the area marked by the yellow box in (c) and Figure S2. (e) Comparison among the enlarged iDPC-STEM image (left), the structural model (middle), and the simulated image (right) of GS-ZM. Scale bar, 1 nm.

“guest wrench” mechanism, by introducing approximately a pair of cation and anion of LiTFSI-EMIMTFSI as guest species (GS) (EMIM: 1-ethyl-3-methylimidazolium, TFSI: bis-(trifluoromethylsulfonyl)imide) into the supercage of LiX zeolite, to fabricate an SE (GS-ZM) with high effective ionic conduction interfacial compatibility. Remarkably, we discover that the Li^+ ions in GS-ZM can be highly activated through the dynamic coordination with the “oxygen wrench” of TFSI^- at room temperature (Figure 1b), as shown by experiments and second-generation Car–Parrinello molecular dynamics (SGCPMD) simulations. Therefore, the restriction of zeolite frameworks toward the framework-associated Li^+ ions can be greatly reduced, which is of great significance to achieve a much more facile ionic mobility compared with pristine ZM, resulting in an $\sim 100\%$ increase in ionic conductivity. It is worth mentioning that the introduced GS are anchored in the supercage by framework-associated Li^+ ions in various directions during this dynamic coordination process and cannot co-migrate with ion carriers, making GS-ZM a single-ion conductor with an outstanding Li^+ transference number of 0.97. When combined with the superior ionic conduction of GS-ZM with the favorable interface structure between GS-ZM and electrodes, the assembled all-solid-state Li -ion and Li -air batteries exhibit state-of-the-art electrochemical performance.

The ionic activation strategy based on the “guest wrench” mechanism opens up fresh avenues for the design of solid electrolytes, and the ultrathin, flexible, nonflammable, and low-cost GS-ZM with remarkable performance provides valuable insight for developing practically accessible all-solid-state energy storage systems.

RESULTS AND DISCUSSION

Fabrication of GS-ZM. The GS was introduced in zeolite via a simple vacuum impregnation process. With an ultralow mass ratio of GS/zeolite (1:8.3), about only one pair of cation and anion of GS is accommodated in each supercage of LiX zeolite (see details in the Supporting Information), achieving the construction of an all-solid-state zeolite-based material. The LiX zeolite ($[(\text{SiAlO}_4)_6\text{Li}_9]_6$, FAU zeolite) is a crystalline inorganic porous solid with an open framework structure consisting of 1:1 corner-sharing $[\text{SiO}_4]$ and $[\text{AlO}_4]$ tetrahedra accompanied by framework-associated Li^+ ions for charge compensation.¹⁷ Considering that supercages of LiX zeolite are 1.3-nm-diameter cavities connected by 12-ring windows with a diameter of 0.74 nm,¹⁸ LiTFSI-EMIMTFSI GS is a suitable guest, as it is difficult for GS to be desorbed from the 12-ring windows with a smaller size. To provide continuous migration paths for Li^+ among the zeolite crystals, a

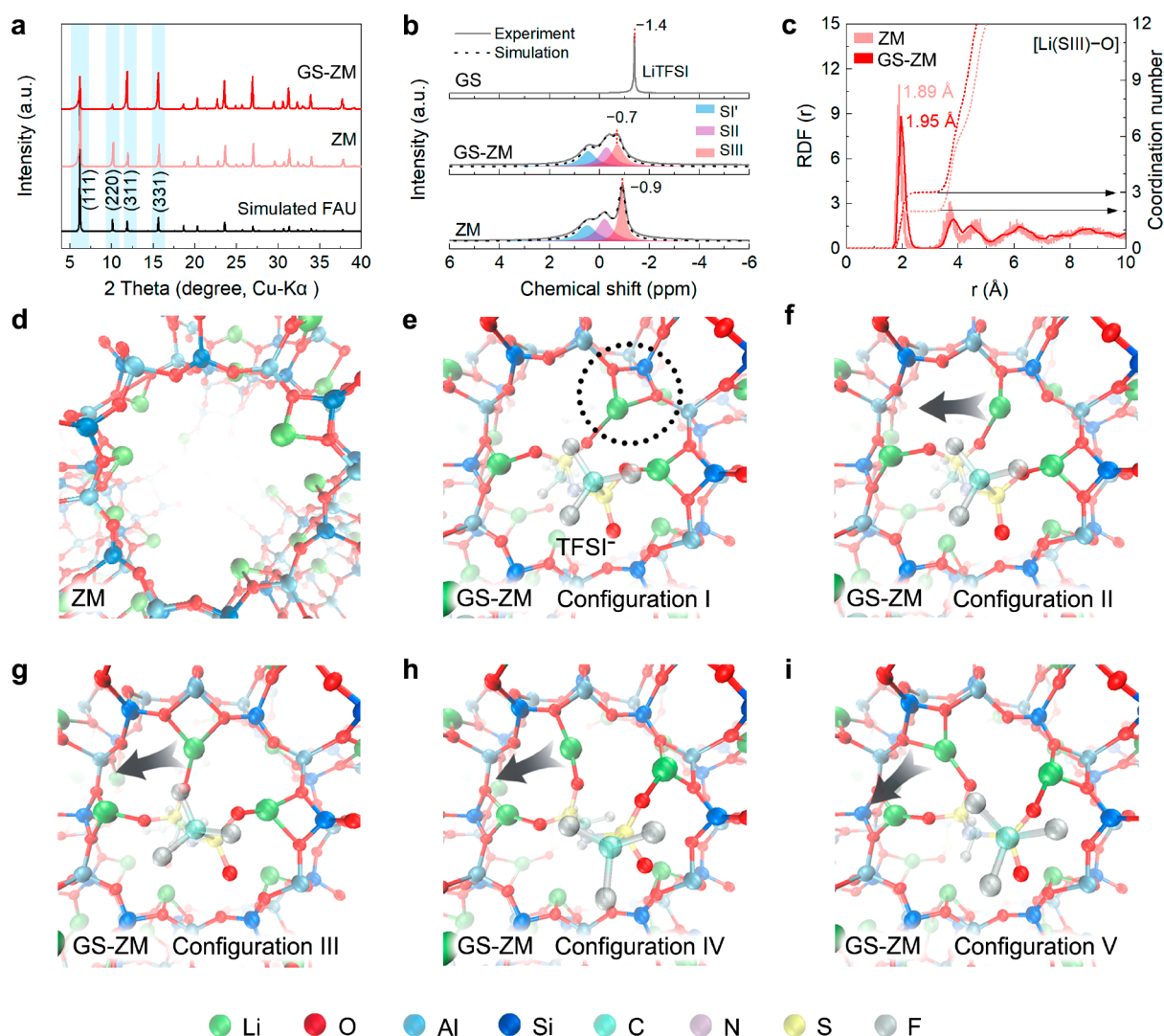


Figure 2. Analysis of host–guest interaction in GS-ZM. (a) XRD patterns of GS-ZM and ZM. The simulated XRD pattern of the FAU structure is provided for comparison. (b) Solid-state ^7Li MAS NMR spectra of GS, GS-ZM, and ZM. (c) Calculated RDFs and the coordination number of Li^+ in ZM and GS-ZM. (d) SGCPMD snapshot of the pristine ZM model. (e–i) SGCPMD snapshots of the Li-ion mobile trajectories in the GS-ZM model.

compact thin ZM with a thickness of $4\ \mu\text{m}$ was prepared via hydrothermal growth and employed as the host to fabricate GS-ZM (Figure S1). The integrated differential phase contrast scanning transmission electron microscopy (iDPC-STEM) image shown in Figure 1c visually reveals the uniform dispersion of GS in the supercage of the LiX zeolite, and the zeolite skeleton remains intact during fabrication. Meanwhile, there is obvious space in each supercage, which indicates that the original continuous state of pristine GS with fluidity has not been maintained. The normalized intensity profile analysis acquired from Figure 1c and Figure S2 also confirms the presence of GS in the zeolite supercage. As shown in the highlighted parts in Figure 1d, the valleys in the black dashed line correspond to the empty cages of the pristine zeolite, and the small peaks in the red line distinctly represent the GS in zeolite host channels.¹⁹ Furthermore, the magnified iDPC-STEM image is in accordance with the simulated iDPC-STEM image acquired from the optimized structural model of GS-ZM with a pair of cation and anion of GS in each supercage of the LiX zeolite (Figure 1e), proving the successful confinement of GS in the zeolite as expected. The results of N_2 adsorption–

desorption, thermogravimetry, and inductively coupled plasma optical emission spectroscopy (ICP-OES) analyses are consistent with those of iDPC-STEM (see details in Figures S3 and S4, Table S1, and supplementary method).

Host–Guest Interaction Enabling Activated Li Ions in GS-ZM. According to X-ray diffraction (XRD) analysis (Figure 2a), the diffractogram of GS-ZM clearly exhibits characteristic peaks of the FAU zeolite. Note that the relative intensities of the diffraction peaks for crystal planes (111), (220), (311), and (331) of GS-ZM are distinct from those of the pristine ZM, implying a redistribution of framework-associated Li ions in the zeolite structure.²⁰ Solid-state ^7Li magic angle spinning nuclear magnetic resonance (^7Li MAS NMR, Figure 2b) was used to analyze the specific occupation sites of Li ions. The ^7Li signal at -1.4 ppm in the NMR spectrum of the original GS with fluidity is attributed to the Li ions that interact with the TFSI^- anions, which cannot be observed in the spectrum of GS-ZM, implying dissociation of the original GS and a redistribution of Li ions in GS-ZM. As for ZM, the ^7Li signals are observed at 0.4, -0.2 , and -0.9 ppm, corresponding to three crystallographic sites: SI' (inside the β -cages in front of

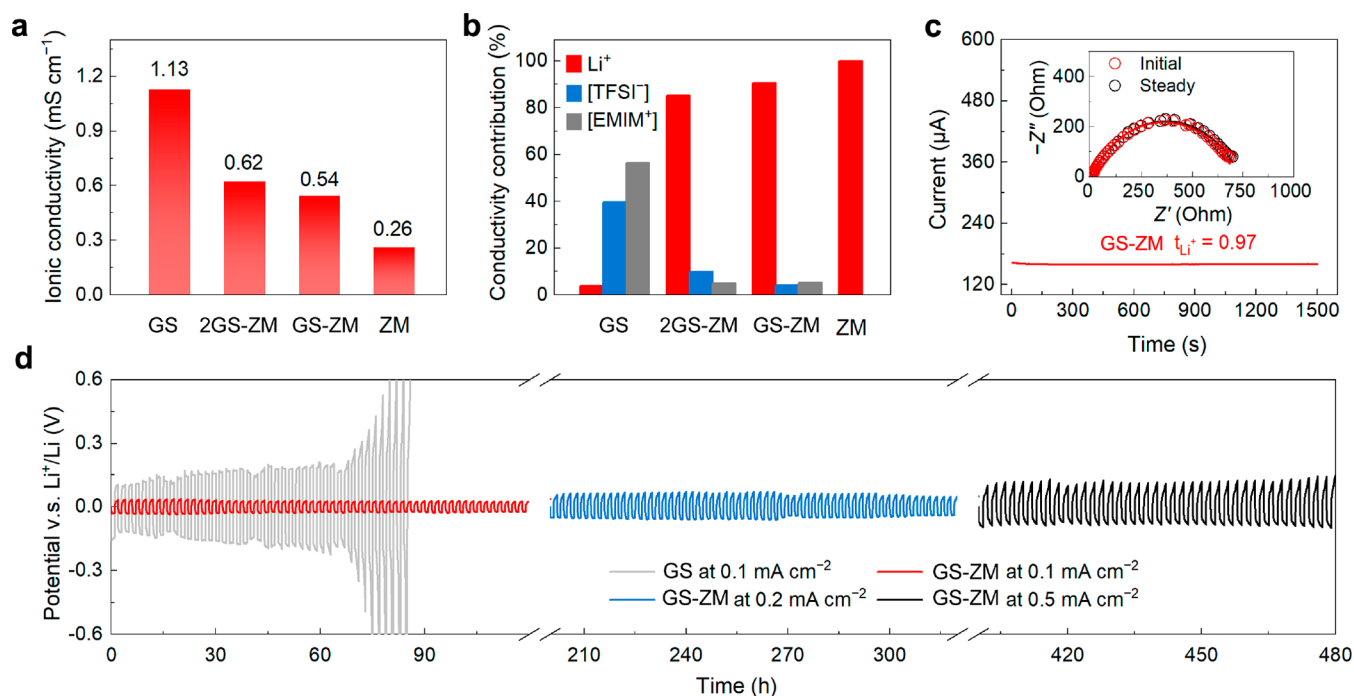


Figure 3. Potential of GS-ZM as a solid electrolyte with fast ionic conduction. (a) Ionic conductivities of GS, 2GS-ZM, GS-ZM, and ZM. (b) Contribution of respective ions to the total conductivity in GS, 2GS@ZM, GS@ZM, and ZM. (c) t_{Li^+} of GS-ZM. (d) Voltage profiles of Li|GS|Li and Li|GS-ZM|Li symmetric cells at current densities of 0.1, 0.2, and 0.5 mA cm⁻².

six-membered-ring (6MR) windows), SII (near the 6MR windows inside supercages), and SIII (near the four-membered-ring (4MR) windows inside supercages) for framework-associated Li ions in LiX zeolite,²¹ respectively. After introducing the GS into ZM, the -0.7 ppm signal manifests that the coordination environment of Li⁺(SIII) in GS-ZM has been significantly changed. On the contrary, the slight change for the signal of Li⁺(SII) and almost no change for the signal of Li⁺(SI') indicate that they are largely unaffected by the GS. Note that Li⁺(SIII) is the primary contributor to the ionic conduction;²² therefore, the introduction of GS can further regulate the ionic transport behavior in GS-ZM.

To gain further understanding of the coordination and mobility of Li-ion carriers in GS-ZM, SGCPMD was conducted based on a GS model (Figure S5a), a ZM model (Figure S5b, Figure 2d), and a GS-ZM model (Figure 2e). The SGCPMD simulation results reveal that the Li⁺(SIII) in the ZM model coordinates with two O of the zeolite framework (Figure 2d). In contrast, the Li⁺(SIII) of GS-ZM interplays with an O of TFSI⁻ ($-S=O$) in GS in addition to coordinating with two O of the zeolite (Figure 2e), which is in accordance with the result of the ⁷Li NMR spectrum and can also be verified by the Fourier-transform infrared (FTIR) spectra^{23,24} (Figure S6). As the Li⁺ contributed by GS can occupy the zeolite framework-associated sites (SIII) by coordinating with TFSI⁻ and the zeolite framework after being introduced (Figure S7 and Video S1), the Li⁺ contributed by GS and the pristine zeolite framework-associated Li⁺(SIII) seem to be equivalent in GS-ZM and undergo the same migration process.

A series of SGCPMD snapshots provide more detailed information about the movement of specific Li⁺. In the simulation of GS-ZM (Figure 2e–i, Video S2), Li⁺(SIII) coordinated with two O of the SiO₄ tetrahedra of zeolite, and

an O of the TFSI⁻ in GS (noted as 2O_{zeolite}-Li-O_{TFSI}) is chosen as an initial configuration (configuration I, Figure 2e). Then, the coordination between the Li⁺ and the O of zeolite can be interrupted by the vibration of the TFSI⁻, forming O_{zeolite}-Li-O_{TFSI} (configuration II, Figure 2f), and the Li⁺ is dragged to a neighbor site, where the Li⁺ coordinates with two O of the AlO₄ tetrahedra of zeolite and an O of the TFSI⁻, forming 2O_{zeolite}-Li-O_{TFSI} (configuration III, Figure 2g). The Li ion does not stop at this site as its final configuration but keeps moving to the next neighbor site, forming 2O_{zeolite}-Li-O_{TFSI} (configuration V, Figure 2i) through an O_{zeolite}-Li-O_{TFSI} transition state (configuration IV, Figure 2h) similar to configuration II. Such motion is shown to be continuous and fast throughout the simulation process at room temperature, resulting in a higher mobility of Li⁺(SIII) in GS-ZM compared to ZM. Simultaneously, TFSI⁻ is restrained by framework-associated Li ions in various directions during this dynamic pulling process, so that TFSI⁻ is anchored in the supercage while promoting ion conduction (Video S2). Unlike the TFSI⁻ anions in GS-ZM, the EMIM⁺ cations in GS-ZM, which are undesirable as ionic carriers, present little impact on the mobile Li⁺ during the simulation, as shown in charge density difference plots (Figure S8). As control groups, the SGCPMD models of original GS and ZM (Figure S5) show that most of the Li ions stay at their original sites with lower mobility during the whole simulation, and only a few Li ions migrate due to thermal excitations.

According to the calculated radial distribution functions (RDFs) and coordination numbers acquired from SGCPMD (Figure 2c), the first-shell integration shows that the Li⁺(SIII) of GS-ZM is coordinated with three adjacent O (two from zeolite and one from TFSI⁻ as mentioned above), which is different from the coordination number of 2 for Li⁺(SIII) in the pristine zeolite. Also, the average atomic distance between Li⁺(SIII) and O changes from 1.89 Å to 1.95 Å after the

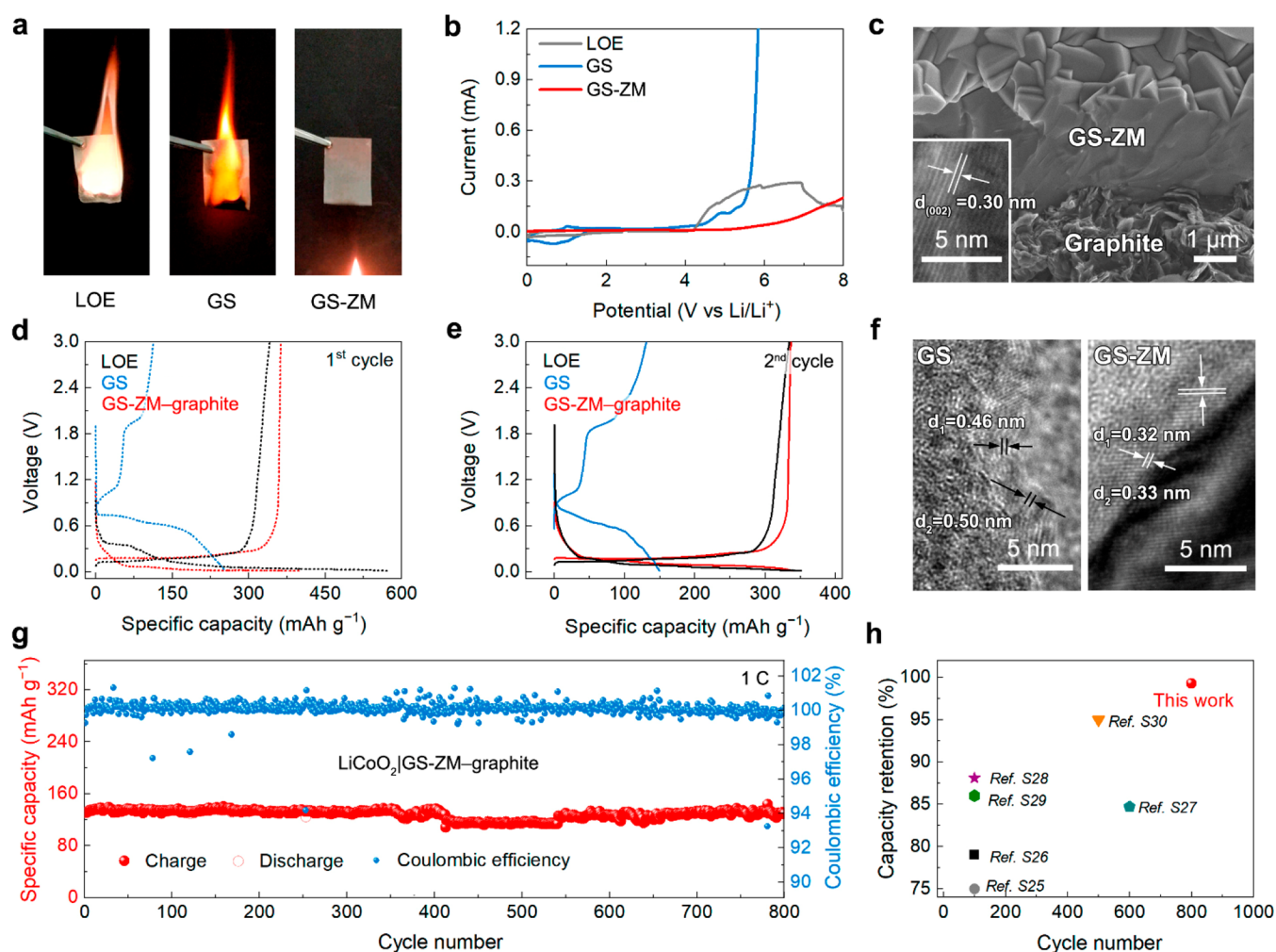


Figure 4. Properties of an all-solid-state Li-ion battery with GS-ZM. (a) Photo images of the flame test on a glass fiber infiltrated by LOE, a glass fiber infiltrated by GS, and a GS-ZM. (b) Electrochemical windows of LOE, GS, and GS-ZM. (c) SEM image of GS-ZM–graphite integrated structure with a TEM image of the graphite anode in the inset. Scale bars, 1 μm (main image); 5 nm (inset). Galvanostatic charge and discharge profiles of half-cells with LOE, GS, and GS-ZM–graphite integrated structure for (d) the 1st and (e) the 2nd cycle at 0.2 C (1 C = 330 mA g^{-1}). (f) TEM images of graphite anodes of Li-ion batteries with GS (left) and GS-ZM (right) after cycling. Scale bars: 5 nm. (g) Cycling performance and Coulombic efficiency of all-solid-state Li-ion batteries with GS-ZM at 1 C. (h) A comparison of the performance of all-solid-state Li-ion batteries reported in the literature and this work.

introduction of GS into ZM. These results indicate that there are more loosely bound Li ions in GS-ZM, which is beneficial for a more facile ionic mobility than that in the pristine ZM.

Consequently, it is clear that GS-ZM possesses activated Li ions with high mobility through the dynamic coordination with the “O wrench” of TFSI[−] at room temperature. Therefore, the GS-ZM is expected to achieve a superior ionic conductive capability.

Electrochemical impedance spectroscopy (EIS) was employed to measure the ionic conductivity of GS-ZM. GS-ZM exhibits an $\sim 100\%$ increase in ionic conductivity (0.54 mS cm^{-1}) in comparison with ZM (0.26 mS cm^{-1}), which benefits from the activation of Li ions based on the “guest wrench” mechanism (Figure 3a). In contrast, the original GS with fluidity displays a higher ionic conductivity of 1.13 mS cm^{-1} . It should be noted that the experimental ionic conductivity of the original GS does not directly reflect the effective migration of Li ions as the expected charge carriers, because the co-migrated TFSI[−] and EMIM⁺ ions also contribute to the ionic conductivity of the original GS.

To further reveal the ionic conduction behavior, the contributions of various ions to the total conductivity of electrolytes were evaluated using molecular dynamics (MD) simulations.²⁵ Although the conductivity results on the basis of MD simulations may not be quantitatively accurate due to the host–guest systems with uncertain fine crystal structure, the qualitative analysis, however, is still insightful for a better understanding of ionic transport in the GS-ZM system. As shown in the conductivity contribution in Figure 3b, the contribution of EMIM⁺ and TFSI[−] to the ionic conductivity of the GS-ZM model is about 9%, which is far below the ratio of 96% in the original GS model. The contribution of Li⁺ to the ionic conductivity of the GS-ZM model (91%) is even comparable to that of the ZM model (100%), of which the conductivity is totally derived from the contribution of Li⁺. These results demonstrate the superior confinement effect of the zeolite toward the EMIM⁺ and TFSI[−] to restrict their undesired co-migration, resulting in a highly effective Li ionic conduction in the GS-ZM model. Therefore, GS-ZM exhibits a lower activation energy (0.13 eV) than that of the original GS

(0.34 eV), as shown in Figure S9. In addition, an ultrahigh Li^+ transference number (t_{Li^+}) of 0.97 has been achieved for GS-ZM (measured based on Evans' method,²⁶ Figure 3c), indicating that GS-ZM can be regarded as a single-ion conductor of Li ions. On the contrary, the original GS suffering from the co-migration of EMIM⁺ and TFSI⁻ ions shows a low t_{Li^+} of only 0.08 (Figure S10). The ultrahigh t_{Li^+} of GS-ZM also indicates that the original continuous state of GS with fluidity has not been maintained in GS-ZM, which possesses a quite different conductive mechanism. It is worth mentioning that GS-ZM is in sharp contrast with the semicomposite SEs constructed by confining LEs in various porous materials. Because the porous materials in these semicomposite SEs mainly act as a matrix to confine the LEs, which remain in the original liquid form, these semicomposite SEs suffer from the co-migration and exhibit a much lower transference number of only 0.13–0.46 (Table S2).

Considering that TFSI⁻ plays a key role in the activation of Li ions, a higher content of GS (about twice as much as the value in GS-ZM, i.e., two pairs of cations and anions of GS in each supercage of LiX zeolite) has been introduced into the ZM to investigate the effect of GS content on ionic conduction (named 2GS-ZM, Figure S11). As shown in Figure 3a, the ionic conductivity increases with the increasing content of GS, whereas the higher experimental value (0.62 mS cm⁻¹) cannot imply the more effective migration of Li ions in 2GS-ZM than in GS-ZM. The interaction effect of zeolite toward guest species may be weakened along with the increasing content of GS in 2GS-ZM due to the reduced average binding energy of framework ions of zeolite toward the single ion of GS and the increased interaction among GS,²⁷ which can also be demonstrated by FTIR (Figure S5). Therefore, the co-migration of EMIM⁺ and TFSI⁻ ions of GS slightly recovers in the 2GS-ZM model, resulting in a lower effective ionic conduction of Li ions (85%) than that of the GS-ZM model (Figure 3b).

To further demonstrate the ionic conduction and stability of GS-ZM as an SE, a symmetric Li cell with GS-ZM (Li|GS-ZM|Li) was assembled, and the common liquid organic electrolyte (LOE) and the original GS were used as electrolytes for comparison. Taking advantage of the highly effective Li^+ ionic conductivity of GS-ZM, the Li|GS-ZM|Li symmetric cell exhibits a lower plating/stripping overpotential (Figure 3d) than the symmetric cell using original GS with high ionic conductivity but low t_{Li^+} (Figure S10). Moreover, the high stability of GS-ZM ensures the pronounced reversibility of fast ionic transport at room temperature, whereas the Li|GS|Li and Li|LOE|Li symmetric cells show inferior cycling performance terminated by serious polarization and short circuits (Figure 3d, Figure S12). The Li|GS-ZM|Li symmetric cell operates stably even under the high current densities of 0.2 and 0.5 mA cm⁻², benefiting from the high ionic conduction and excellent electrochemical stability.²⁸ Furthermore, the low electronic conductivity of 4.7×10^{-10} S cm⁻¹ of GS-ZM (Figure S13) reduces the risk of nucleation and growth of lithium dendrites inside the solid electrolyte^{29,30} and short circuits.

Adaptability of GS-ZM in All-Solid-State Batteries.

The compatibility of the SEs in various all-solid-state battery systems is of great significance for practical application. As shown in Figure S14, the flexible GS-ZM can be easily scaled up in the laboratory. Regarding the safety issue, the GS-ZM presents an excellent flame-retardant property in the flame

tests, in stark contrast to the LOE and original GS (Figure 4a). In addition, GS-ZM exhibits fairly high electrochemical stability with a voltage window of 0–5.0 V, far beyond those of LOE (2.0–4.2 V) and original GS (1.8–3.8 V), as shown in Figure 4b. The broadened electrochemical voltage window of the GS-ZM renders high adaptability in various battery systems.

A widely commercialized Li-ion battery system with a lithium cobalt oxide (LiCoO₂) cathode and graphite anode was selected to demonstrate the application potential of GS-ZM as an SE. First, an SE–anode integrated structure with GS-ZM and graphite anode (GS-ZM–graphite) was constructed to ensure a superior interfacial contact. The scanning electron microscopy (SEM) image (main image in Figure 4c) shows that GS-ZM with a thickness of about 4 μm is firmly integrated with the graphite anode by the in situ growth of GS-ZM, and the graphite remains intact in shape. The structural integrity of the graphite in GS-ZM–graphite is further verified according to the approximate intensity ratio of the two peaks belonging to D and G bands compared with the pristine graphite in Raman spectra (Figure S15). To evaluate the electrochemical behavior of the graphite anode, a half-cell was assembled with heat-softened Li metal on the other side of GS-ZM as the counter electrode. The half-cell with the GS-ZM–graphite integrated structure exhibits typical charge and discharge profiles of graphite with a specific capacity of 340 mAh g⁻¹ (Figure 4d and e), which is much higher than that of the half-cell with GS (150 mAh g⁻¹) and comparable with that of the half-cell with LOE (352 mAh g⁻¹). Also, the Coulombic efficiency of the half-cell with a GS-ZM–graphite integrated structure is much higher than that of the half-cell with LOE, further demonstrating the high stability of GS-ZM. Note that the electrochemical behavior of the half-cell with GS-ZM is significantly different from that of the half-cell using original GS, in which the ions of original GS could co-insert with Li ions into graphite lattices owing to the co-migration issue.³¹ The transmission electron microscopy (TEM) image (left image in Figure 4f) provides visual evidence that the lattice fringe spacing distance of graphite cycled in the battery with original GS distinctly increases compared with that of the pristine graphite (inset image in Figure 4c), indicating irreversible damage of the graphite anode and thus severe decay of electrochemical performance. In contrast, the microstructure of the graphite cycled in the battery with GS-ZM basically remains (right image in Figure 4f), revealing that the fabrication of GS-ZM can not only restrict the undesired co-migration of GS cations but also ensure the facile conduction of Li ions. Then, the all-solid-state full cell (LiCoO₂|GS-ZM–graphite) was assembled using commercial LiCoO₂ as the cathode material, and it presents an excellent rate capability (Figure S16) and a stable cyclic performance for over 800 cycles at 1 C, achieving a high capacity retention up to 99.3% without significant decay of Coulombic efficiency (~99.8%, Figure 4g), in sharp contrast with the battery using the original GS (Figure S17) and other all-solid-state Li-ion batteries reported in previous literature (Figure 4h and Table S3). The impressive cycle life is mainly due to the high electrochemical stability of GS-ZM and the superior interfacial compatibility of GS-ZM toward electrodes.^{32–34} To verify the compatibility of SE fabricated based on the “guest wrench” in zeolite strategy in other metal-ion batteries, a NaGS–NaZM solid electrolyte (Figure S18) was fabricated by introducing NaTFSI–EMIMTFSI GS (NaGS) into the zeolite membrane

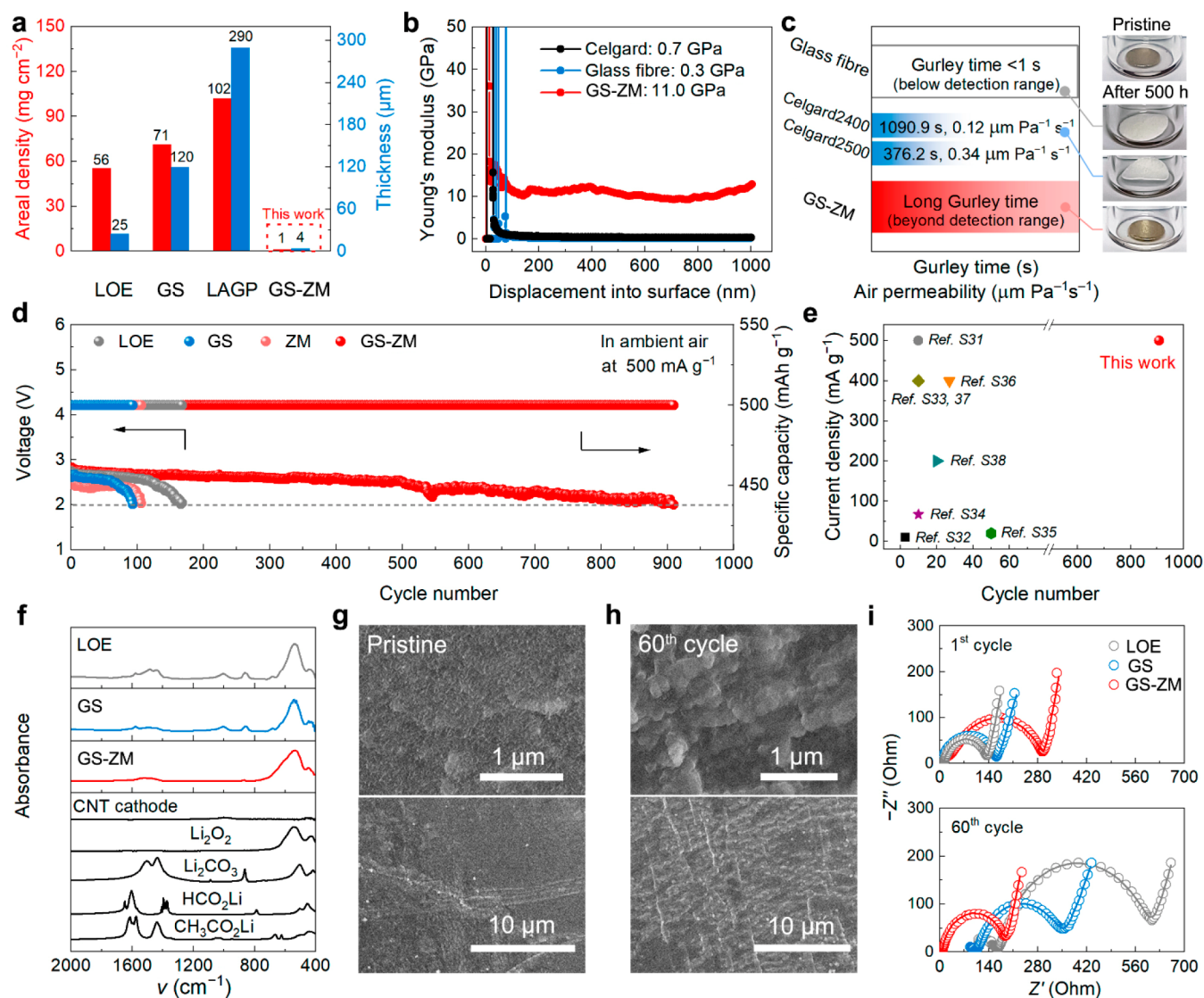


Figure 5. Properties of all-solid-state Li–air batteries with GS-ZM. (a) Areal density and thickness of electrolyte layers in the batteries using LOE, GS, LAGP, and GS-ZM. (b) Elastic modulus and depth-dependent elastic modulus tests of GS-ZM, glass fiber, and Celgard separators. (c) Gurley time and air permeability values for Celgard, glass fiber separators, and GS-ZM, accompanied by optical images of lithium metal inserted in the test devices sealed with Celgard, glass fiber separators, and GS-ZM. (d) Cycling performance of Li–air batteries with LOE, GS, and all-solid-state Li–air batteries with ZM and GS-ZM at 500 mA g⁻¹. (e) A comparison of the performance of all-solid-state Li–air batteries reported in previous literature and this work. (f) FTIR spectra of discharge products in the batteries with GS and GS-ZM. SEM images of (g) the pristine Li metal anode and (h) the Li metal anode after 60 cycles in the battery with GS-ZM. Scale bars: 1 μm (top images); 10 μm (bottom images). (i) EIS spectra of Li–air batteries with LOE, GS, and GS-ZM after cycling.

without Li-ion exchange (NaZM). The all-solid-state Na-ion battery using NaGS–NaZM also exhibits better electrochemical performance than that using NaGS, indicating a promising compatibility of GS-ZM SEs in various systems^{35,36} (Figure S19).

Beyond Li-ion batteries, Li–air batteries with the highest theoretical energy density are expected to be the most prominent secondary batteries for next-generation energy storage,^{37,38} whereas the construction and the stable operation of all-solid-state Li–air batteries in ambient air remain formidable challenges. First, the practical energy density of the Li–air battery is fairly low compared with its theoretical value due to the excessive mass and volume of the inert electrolyte part. Compared with liquid and solid electrolytes including LOE, GS, and NASICON-type Li_{1.5}Al_{0.5}Ge_{1.5}P₃O₁₂ (LAGP), the ultrathin GS-ZM with relatively lower mass and

volume (1.2 mg cm⁻², 4 μm) endows its promising prospects in constructing high-energy-density energy storage devices (Figure 5a). With a Li metal anode, Li–air batteries suffer from the problem of lithium-dendrite growth.⁶ The solid electrolyte GS-ZM with compact and continuous structure displays an average Young's modulus of 11.0 GPa (Figure 5b), far beyond those of glass fiber (0.3 GPa) and Celgard separators (0.7 GPa), and thus can effectively prevent the growth of lithium dendrites and battery short-circuit accidents.³⁹ In addition to the dendrite issue, the hyperactive Li metal anode is susceptible to corrosion by the air components in open-structured Li–air batteries.⁴⁰ Benefiting from the dense structure and the modified pores, GS-ZM exhibits an ultralong Gurley time even beyond the detection limit (left image in Figure 5c), indicating the ultraslow air permeation through GS-ZM.³⁹ Consequently, the Li metal sealed with GS-ZM can

be effectively protected after being exposed to the air for long periods of time, in sharp contrast with the Li metal sealed with glass fiber and Celgard separators that are generally used in batteries based on LEs (right images in Figure 5c). Additionally, combining such a dense SE layer with a superhydrophobic cathode, such as porous carbon nanotubes (CNTs), can further ensure the stable operation of the open-structured Li–air batteries in ambient air.⁴¹ Herein, hydrophobic CNTs were employed as the cathode to construct integrated all-solid-state Li–air batteries by the in situ growth of GS-ZM on a CNT cathode, forming a CNT–GS-ZM integrated structure (Figure S20 and Figure S21).^{15,42}

Reversibility and stability of the all-solid-state Li–air batteries with GS-ZM were demonstrated by the galvanostatic charge and discharge measurement at a series of current densities of 0.1, 0.2, 0.5, 1, and 2 A g⁻¹ in ambient air. As shown in Figure S22, the Li–air battery with GS-ZM exhibits a relatively low overpotential of ~1.6 V at 2 A g⁻¹, and the overpotential recovers to ~1.0 V when the current density rapidly reduces to 0.1 A g⁻¹. Remarkably, despite the fluidity of the original GS, the rate capability of the battery with GS-ZM is far superior to that of the battery with the original GS, in which the overpotential increases sharply along with the increasing current density (up to 3.5 V at 2 A g⁻¹). Moreover, the all-solid-state Li–air battery with GS-ZM demonstrates 909 cycles at 500 mA g⁻¹ in ambient air (Figure 5d), which is far superior to those of Li–air batteries with original GS (93 cycles), commercial LOE (168 cycles), and the all-solid-state Li–air battery with pristine ZM (106 cycles). Such remarkable performance of the all-solid-state Li–air battery with GS-ZM is due to the high stability and the fast Li⁺ conduction of GS-ZM, as well as the enhanced interfacial compatibility and better protection of the Li metal anode. As a result, the all-solid-state Li–air battery with GS-ZM exhibits extraordinary electrochemical stability under various operating conditions in ambient air (Figure S23), which is the best cycling stability reported to date in all-solid-state Li–air batteries (Figure 5e and Table S4).

The SEM image shows that discharge products with slim-film-like morphology are uniformly formed on the cathode in the all-solid-state Li–air battery with GS-ZM (Figure S24). Such film-like morphology has been proved to be favorable for the facile decomposition of discharge products,⁴³ enhancing the reversibility of the Li–air battery. Subsequently, the composition of the discharge product was determined by FTIR spectra. As shown in Figure 5f, Li₂O₂ is the major discharge product with the absence of byproducts such as HCO₂Li and CH₃CO₂Li in the battery using GS-ZM, revealing high electrochemical and chemical stability of the battery using GS-ZM compared with the battery using original GS and LOE.³⁷ As for the anode side, SEM images show that the surface of the Li metal anode in the Li–air batteries with GS-ZM after being cycled for 60 times is relatively smooth compared with the cases in LOE- and GS-based systems (Figure 5g,h and Figure S25). This morphology indicates that the compact GS-ZM with high stability and mechanical strength not only prevents corrosion toward the Li metal anode but also suppresses the growth of Li dendrites.^{44,45} Additionally, the Li metal anode tends to fit the surface topography of the GS-ZM during Li plating/stripping processes, achieving a better contact between the anode and the SE to reduce the impedance of the battery. Electrochemical impedance spectra further verify the enhanced interfacial

compatibility, as the impedance of the all-solid-state Li–air battery with GS-ZM slightly decreases after 60 cycles (Figure 5i). In contrast, although the batteries using LEs possess lower impedance in comparison with the all-solid-state battery based on GS-ZM after the first cycle, the decomposition of unstable LEs and the corrosion of the metal anode upon charging and discharging significantly increase the impedance of the battery, resulting in inferior electrochemical performance. Furthermore, an X-ray photoelectron spectroscopy (XPS) survey and Li 1s, Al 2p, and Si 2p spectra (Figure S26) of pristine GS-ZM and GS-ZM after 60 cycles show that the structure and the element state of GS-ZM remain unchanged after cycling, indicating the stability of GS-ZM against Li metal anodes.

CONCLUSIONS

In summary, a facile “guest wrench” in zeolite strategy has been proposed to fabricate a GS-ZM solid electrolyte for all-solid-state energy storage systems with outstanding performance, high safety, and low cost. As the host, zeolite plays a key role in dispersing and coordinating with the ions of GS, providing a facile migration path for ion carriers and restricting the undesired comigration of GS. Strikingly, the framework-associated Li ions in GS-ZM can be activated through the dynamic coordination with the “oxygen wrench” of TFSI⁻ in GS at room temperature, resulting in an ~100% increase in ionic conductivity compared with ZM, and GS-ZM can be regarded as a single ion conductor with an outstanding Li⁺ transference number of 0.97. The assembled all-solid-state batteries based on GS-ZM electrolytes exhibit remarkable performance, superior to those of the batteries with liquid electrolytes in various energy storage systems. The “guest wrench” in zeolite strategy provides a pathway to enable the highly effective ionic transport of solid electrolytes and is expected to further promote the development of all-solid-state energy storage systems with excellent performance, high energy density, and low cost.

ASSOCIATED CONTENT

Supporting Information

The Supporting Information is available free of charge at <https://pubs.acs.org/doi/10.1021/jacs.3c07858>.

Additional experimental details for the synthesis and characterization (XRD patterns, SEM, iDPC-STEM, TEM images, N₂ adsorption–desorption isotherms, thermogravimetric curves, FTIR and Raman spectra), computational details, SGCPMD snapshots, charge density difference calculation results, additional electrochemical data, and performance comparison of different batteries (PDF)

Dynamic state of the Li ions of guest species after being introduced into the zeolite via SGCPMD simulation (MP4)

Ionic activation mechanism for ion carriers in GS-ZM zeolite solid electrolyte via SGCPMD simulation (MP4)

AUTHOR INFORMATION

Corresponding Authors

Jiaao Wang – Department of Chemistry and the Oden Institute for Computational Engineering and Sciences, The University of Texas at Austin, Austin, Texas 78712-0165, United States; orcid.org/0000-0002-4944-4951; Email: wangjiaao0720@utexas.edu

Jihong Yu – State Key Laboratory of Inorganic Synthesis and Preparative Chemistry, College of Chemistry, Jilin University, Changchun 130012, People's Republic of China; International Center of Future Science, Jilin University, Changchun 130012, People's Republic of China; orcid.org/0000-0003-1615-5034; Email: jihong@jlu.edu.cn

Authors

Xiwen Chi – State Key Laboratory of Inorganic Synthesis and Preparative Chemistry, College of Chemistry, Jilin University, Changchun 130012, People's Republic of China; International Center of Future Science, Jilin University, Changchun 130012, People's Republic of China

Malin Li – State Key Laboratory of Inorganic Synthesis and Preparative Chemistry, College of Chemistry, Jilin University, Changchun 130012, People's Republic of China; International Center of Future Science, Jilin University, Changchun 130012, People's Republic of China; orcid.org/0000-0002-6736-180X

Xiao Chen – Beijing Key Laboratory of Green Chemical Reaction Engineering and Technology, Department of Chemical Engineering, Tsinghua University, Beijing 100084, People's Republic of China; orcid.org/0000-0003-1104-6146

Jun Xu – National Centre for Magnetic Resonance in Wuhan, State Key Laboratory of Magnetic Resonance and Atomic and Molecular Physics, Innovation Academy for Precision Measurement Science and Technology, Chinese Academy of Sciences, Wuhan 430071, People's Republic of China; orcid.org/0000-0003-2741-381X

Xin Yin – State Key Laboratory of Inorganic Synthesis and Preparative Chemistry, College of Chemistry, Jilin University, Changchun 130012, People's Republic of China

Shanghua Li – State Key Laboratory of Inorganic Synthesis and Preparative Chemistry, College of Chemistry, Jilin University, Changchun 130012, People's Republic of China; International Center of Future Science, Jilin University, Changchun 130012, People's Republic of China

Ziyue Jin – State Key Laboratory of Inorganic Synthesis and Preparative Chemistry, College of Chemistry, Jilin University, Changchun 130012, People's Republic of China

Zhaodi Luo – State Key Laboratory of Inorganic Synthesis and Preparative Chemistry, College of Chemistry, Jilin University, Changchun 130012, People's Republic of China

Xingxing Wang – State Key Laboratory of Inorganic Synthesis and Preparative Chemistry, College of Chemistry, Jilin University, Changchun 130012, People's Republic of China; National Centre for Magnetic Resonance in Wuhan, State Key Laboratory of Magnetic Resonance and Atomic and Molecular Physics, Innovation Academy for Precision Measurement Science and Technology, Chinese Academy of Sciences, Wuhan 430071, People's Republic of China

Dechen Kong – State Key Laboratory of Inorganic Synthesis and Preparative Chemistry, College of Chemistry, Jilin University, Changchun 130012, People's Republic of China

Meng Han – State Key Laboratory of Inorganic Synthesis and Preparative Chemistry, College of Chemistry, Jilin University, Changchun 130012, People's Republic of China

Ji-Jing Xu – State Key Laboratory of Inorganic Synthesis and Preparative Chemistry, College of Chemistry, Jilin University, Changchun 130012, People's Republic of China; International Center of Future Science, Jilin University,

Changchun 130012, People's Republic of China;

orcid.org/0000-0002-6212-8224

Zonghang Liu – School of Science and Engineering, Shenzhen Key Laboratory of Functional Aggregate Materials, The Chinese University of Hong Kong, Shenzhen, Guangdong 518172, People's Republic of China

Donghai Mei – School of Environmental Science and Engineering, Tiangong University, Tianjin 300387, People's Republic of China; orcid.org/0000-0002-0286-4182

Graeme Henkelman – Department of Chemistry and the Oden Institute for Computational Engineering and Sciences, The University of Texas at Austin, Austin, Texas 78712-0165, United States; orcid.org/0000-0002-0336-7153

Complete contact information is available at:

<https://pubs.acs.org/10.1021/jacs.3c07858>

Author Contributions

X. Chi and M. Li contributed equally.

Notes

The authors declare no competing financial interest.

Both national and international patent applications have been made regarding the data obtained in the related study. The national patent application number made to the Chinese Patent Institute is CN202311013483.4, and the international patent application number is PCT/CN2023/117384.

ACKNOWLEDGMENTS

We thank the National Natural Science Foundation of China (Grants 22288101, 21920102005, 21835002, and 22109050) and the 111 Project (B17020) for supporting this work. Calculations at UT Austin were supported by the Welch Foundation (F-1841), the Texas Advanced Computing Center, and the National Energy Scientific Research Center.

REFERENCES

- Armand, M.; Tarascon, J.-M. Building Better Batteries. *Nature* **2008**, *451*, 652–657.
- Liu, J.; Ye, C.; Wu, H.; Jaroniec, M.; Qiao, S.-Z. 2D Mesoporous Zincophilic Sieve for High-Rate Sulfur-Based Aqueous Zinc Batteries. *J. Am. Chem. Soc.* **2023**, *145*, 5384–5392.
- Manthiram, A.; Yu, X.; Wang, S. Lithium Battery Chemistries Enabled by Solid-State Electrolytes. *Nat. Rev. Mater.* **2017**, *2*, 16103.
- Lai, J.; Xing, Y.; Chen, N.; Li, L.; Wu, F.; Chen, R. Electrolytes for Rechargeable Lithium-Air Batteries. *Angew. Chem., Int. Ed.* **2020**, *59*, 2974–2997.
- Famprikis, T.; Canepa, P.; Dawson, J. A.; Islam, M. S.; Masquelier, C. Fundamentals of Inorganic Solid-State Electrolytes for Batteries. *Nat. Mater.* **2019**, *18*, 1278–1291.
- Liu, Y.; Li, C.; Li, B.; Song, H.; Cheng, Z.; Chen, M.; He, P.; Zhou, H. Germanium Thin Film Protected Lithium Aluminum Germanium Phosphate for Solid-State Li Batteries. *Adv. Energy Mater.* **2018**, *8*, 1702374.
- Liu, Y.; He, P.; Zhou, H. Rechargeable Solid-State Li-Air and Li-S Batteries: Materials, Construction, and Challenges. *Adv. Energy Mater.* **2018**, *8*, 1701602.
- Chen, R.; Li, Q.; Yu, X.; Chen, L.; Li, H. Approaching Practically Accessible Solid-State Batteries: Stability Issues Related to Solid Electrolytes and Interfaces. *Chem. Rev.* **2020**, *120*, 6820–6877.
- Fan, L.-Z.; He, H.; Nan, C.-W. Tailoring Inorganic-Polymer Composites for the Mass Production of Solid-State Batteries. *Nat. Rev. Mater.* **2021**, *6*, 1003–1019.
- Yu, X.; Grundish, N. S.; Goodenough, J. B.; Manthiram, A. Ionic Liquid (IL) Laden Metal-Organic Framework (IL-Mof) Electrolyte for Quasi-Solid-State Sodium Batteries. *ACS Appl. Mater. Interfaces* **2021**, *13*, 24662–24669.

- (11) Tian, X.; Chen, S.; Zhang, P.; Yang, P.; Yi, Y.; Wang, T.; Fang, B.; Liu, P.; Qu, L.; Li, M.; Ma, H. Covalent Organic Frameworks with Immobilized Anions to Liberate Lithium Ions: Quasi-Solid Electrolytes with Enhanced Rate Capabilities. *Electrochim. Acta* **2021**, *389*, 138585.
- (12) Wang, H.; Hood, Z. D.; Xia, Y.; Liang, C. Fabrication of Ultrathin Solid Electrolyte Membranes of B-Li₃PS₄ Nanoflakes by Evaporation-Induced Self-Assembly for All-Solid-State Batteries. *J. Mater. Chem. A* **2016**, *4*, 8091–8096.
- (13) Chang, Z.; Yang, H.; Zhu, X.; He, P.; Zhou, H. A Stable Quasi-Solid Electrolyte Improves the Safe Operation of Highly Efficient Lithium-Metal Pouch Cells in Harsh Environments. *Nat. Commun.* **2022**, *13*, 1510.
- (14) Chi, X.; Li, M.; Di, J.; Bai, P.; Song, L.; Wang, X.; Li, F.; Liang, S.; Xu, J.; Yu, J. A Highly Stable and Flexible Zeolite Electrolyte Solid-State Li-Air Battery. *Nature* **2021**, *592*, 551–557.
- (15) Li, M.; Chi, X.; Yu, J. Zeolite-Based Electrolytes: A Promising Choice for Solid-State Batteries. *PRX Energy* **2022**, *1*, 031001.
- (16) Li, Y.; Yu, J. Emerging Applications of Zeolites in Catalysis, Separation and Host-Guest Assembly. *Nat. Rev. Mater.* **2021**, *6*, 1156–1174.
- (17) Freeman, D. C.; Stamires, D. N. Electrical Conductivity of Synthetic Crystalline Zeolites. *J. Chem. Phys.* **1961**, *35*, 799–806.
- (18) Simon, U.; Flesch, U. Cation-Cation Interaction in Dehydrated Zeolites X and Y Monitored by Modulus Spectroscopy. *J. Porous Mater.* **1999**, *6*, 33–40.
- (19) Shen, B.; Chen, X.; Wang, H.; Xiong, H.; Bosch, E. G. T.; Lazic, I.; Cai, D.; Qian, W.; Jin, S.; Liu, X.; Han, Y.; Wei, F. A Single-Molecule Van Der Waals Compass. *Nature* **2021**, *592*, 541–544.
- (20) Ntais, S.; Moschovi, A. M.; Paloukis, F.; Neophytides, S.; Burganos, V. N.; Dracopoulos, V.; Nikolakis, V. Preparation and Ion Transport Properties of Nay Zeolite-Ionic Liquid Composites. *J. Power Sources* **2011**, *196*, 2202–2210.
- (21) Feuerstein, M.; Lobo, R. Characterization of Li Cations in Zeolite Lix by Solid-State NMR Spectroscopy and Neutron Diffraction. *Chem. Mater.* **1998**, *10*, 2197–2204.
- (22) Feuerstein, M.; Lobo, R. F. Mobility of Li Cations in X Zeolites Studied by Solid-State NMR Spectroscopy. *Solid State Ionics* **1999**, *118*, 135–139.
- (23) Mosa, J.; Velez, J. F.; Aparicio, M. Blend Hybrid Solid Electrolytes Based on LiTFSI Doped Silica-Polyethylene Oxide for Lithium-Ion Batteries. *Membranes* **2019**, *9*, 109.
- (24) Mozshukhina, N.; Tesio, A. Y.; De Leo, L. P. M.; Calvo, E. J. In Situ Infrared Spectroscopy Study of PYR₁₄TFSI Ionic Liquid Stability for Li-O₂ Battery. *J. Electrochem. Soc.* **2017**, *164*, A518–A523.
- (25) Wan, J.; Xie, J.; Kong, X.; Liu, Z.; Liu, K.; Shi, F.; Pei, A.; Chen, H.; Chen, W.; Chen, J.; Zhang, X.; Zong, L.; Wang, J.; Chen, L. Q.; Qin, J.; Cui, Y. Ultrathin, Flexible, Solid Polymer Composite Electrolyte Enabled with Aligned Nanoporous Host for Lithium Batteries. *Nat. Nanotechnol.* **2019**, *14*, 705–711.
- (26) Evans, J.; Vincent, A. C.; Bruce, P. G. Electrochemical Measurement of Transference Numbers in Polymer Electrolytes. *Polymer* **1987**, *28*, 2324–2328.
- (27) Yoshida, Y.; Fujie, K.; Lim, D. W.; Ikeda, R.; Kitagawa, H. Superionic Conduction over a Wide Temperature Range in a Metal-Organic Framework Impregnated with Ionic Liquids. *Angew. Chem., Int. Ed.* **2019**, *58*, 10909–10913.
- (28) Zhu, L.; Wang, Y.; Chen, J.; Li, W.; Wang, T.; Wu, J.; Han, S.; Xia, Y.; Wu, Y.; Wu, M.; Wang, F.; Zheng, Y.; Peng, L.; Liu, J.; Chen, L.; Tang, W. Enhancing Ionic Conductivity in Solid Electrolyte by Relocating Diffusion Ions to Under-Coordination Sites. *Sci. Adv.* **2022**, *8*, No. eabj7698.
- (29) Han, F.; Westover, A. S.; Yue, J.; Fan, X.; Wang, F.; Chi, M.; Leonard, D. N.; Dudney, N. J.; Wang, H.; Wang, C. High Electronic Conductivity as the Origin of Lithium Dendrite Formation within Solid Electrolytes. *Nat. Energy* **2019**, *4*, 187–196.
- (30) Zhou, L.; Zuo, T.-T.; Kwok, C. Y.; Kim, S. Y.; Assoud, A.; Zhang, Q.; Janek, J.; Nazar, L. F. High Areal Capacity, Long Cycle Life 4 V Ceramic All-Solid-State Li-Ion Batteries Enabled by Chloride Solid Electrolytes. *Nat. Energy* **2022**, *7*, 83–93.
- (31) Hyun, W. J.; Thomas, C. M.; Luu, N. S.; Hersam, M. C. Layered Heterostructure Ionogel Electrolytes for High-Performance Solid-State Lithium-Ion Batteries. *Adv. Mater.* **2021**, *33*, 2007864.
- (32) Park, K. H.; Oh, D. Y.; Choi, Y. E.; Nam, Y. J.; Han, L.; Kim, J. Y.; Xin, H.; Lin, F.; Oh, S. M.; Jung, Y. S. Solution-Processable Glass LiI-Li₄SnS₄ Superionic Conductors for All-Solid-State Li-Ion Batteries. *Adv. Mater.* **2016**, *28*, 1874–1883.
- (33) Wang, L.; Chen, B.; Ma, J.; Cui, G.; Chen, L. Reviving Lithium Cobalt Oxide-Based Lithium Secondary Batteries-toward a Higher Energy Density. *Chem. Soc. Rev.* **2018**, *47*, 6505–6602.
- (34) Tan, D. H. S.; Chen, Y. T.; Yang, H.; Bao, W.; Sreenarayanan, B.; Doux, J. M.; Li, W.; Lu, B.; Ham, S. Y.; Sayahpour, B.; Scharf, J.; Wu, E. A.; Deysher, G.; Han, H. E.; Hah, H. J.; Jeong, H.; Lee, J. B.; Chen, Z.; Meng, Y. S. Carbon-Free High-Loading Silicon Anodes Enabled by Sulfide Solid Electrolytes. *Science* **2021**, *373*, 1494–1499.
- (35) Zhong, Y.; Shi, Q.; Zhu, C.; Zhang, Y.; Li, M.; Francisco, J. S.; Wang, H. Mechanistic Insights into Fast Charging and Discharging of the Sodium Metal Battery Anode: A Comparison with Lithium. *J. Am. Chem. Soc.* **2021**, *143*, 13929–13936.
- (36) Ye, C.; Shan, J.; Chao, D.; Liang, P.; Jiao, Y.; Hao, J.; Gu, Q.; Davey, K.; Wang, H.; Qiao, S.-Z. Catalytic Oxidation of K₂S via Atomic Co and Pyridinic N Synergy in Potassium-Sulfur Batteries. *J. Am. Chem. Soc.* **2021**, *143*, 16902–16907.
- (37) Bruce, P. G.; Freunberger, S. A.; Hardwick, L. J.; Tarascon, J. M. Li-O₂ and Li-S Batteries with High Energy Storage. *Nat. Mater.* **2012**, *11*, 19–29.
- (38) Lu, Y.-C.; Gallant, B. M.; Kwabi, D. G.; Harding, J. R.; Mitchell, R. R.; Whittingham, M. S.; Shao-Horn, Y. Lithium-Oxygen Batteries: Bridging Mechanistic Understanding and Battery Performance. *Energy Environ. Sci.* **2013**, *6*, 750–768.
- (39) Liang, W.; Lian, F.; Meng, N.; Lu, J.; Ma, L.; Zhao, C.-Z.; Zhang, Q. Adaptive Formed Dual-Phase Interface for Highly Durable Lithium Metal Anode in Lithium-Air Batteries. *Energy Storage Mater.* **2020**, *28*, 350–356.
- (40) Kim, B. G.; Kim, J.-S.; Min, J.; Lee, Y.-H.; Choi, J. H.; Jang, M. C.; Freunberger, S. A.; Choi, J. W. A Moisture- and Oxygen-Impermeable Separator for Aprotic Li-O₂ Batteries. *Adv. Funct. Mater.* **2016**, *26*, 1747–1756.
- (41) Yang, X. Y.; Xu, J. J.; Chang, Z. W.; Bao, D.; Yin, Y. B.; Liu, T.; Yan, J. M.; Liu, D. P.; Zhang, Y.; Zhang, X. B. Blood-Capillary-Inspired, Free-Standing, Flexible, and Low-Cost Super-Hydrophobic N-CNTs@SS Cathodes for High-Capacity, High-Rate, and Stable Li-Air Batteries. *Adv. Energy Mater.* **2018**, *8*, 1702242.
- (42) Xiao, Y.; Turcheniuk, K.; Narla, A.; Song, A. Y.; Ren, X.; Magasinski, A.; Jain, A.; Huang, S.; Lee, H.; Yushin, G. Electrolyte Melt Infiltration for Scalable Manufacturing of Inorganic All-Solid-State Lithium-Ion Batteries. *Nat. Mater.* **2021**, *20*, 984–990.
- (43) Jeong, Y. S.; Park, J. B.; Jung, H. G.; Kim, J.; Luo, X.; Lu, J.; Curtiss, L.; Amine, K.; Sun, Y. K.; Scrosati, B.; Lee, Y. J. Study on the Catalytic Activity of Noble Metal Nanoparticles on Reduced Graphene Oxide for Oxygen Evolution Reactions in Lithium-Air Batteries. *Nano Lett.* **2015**, *15*, 4261–4268.
- (44) Xu, R.; Liu, F.; Ye, Y.; Chen, H.; Yang, R. R.; Ma, Y.; Huang, W.; Wan, J.; Cui, Y. A Morphologically Stable Li/Electrolyte Interface for All-Solid-State Batteries Enabled by 3D-Micropatterned Garnet. *Adv. Mater.* **2021**, *33*, 2104009.
- (45) Deng, T.; Ji, X.; Zou, L.; Chiekezi, O.; Cao, L.; Fan, X.; Adebisi, T. R.; Chang, H. J.; Wang, H.; Li, B.; Li, X.; Wang, C.; Reed, D.; Zhang, J. G.; Sprenkle, V. L.; Wang, C.; Lu, X. Interfacial-Engineering-Enabled Practical Low-Temperature Sodium Metal Battery. *Nat. Nanotechnol.* **2022**, *17*, 269–277.